Check for updates

Exploring the role of Mn²⁺ in the structure, magnetic properties, and radar absorption performance of MnₓFe₃₋ₓO₄–DEA/MWCNT nanocomposites

Wida Puteri Agista,[a] ST. Ulfawanti Intan Subadra,[a] Ahmad Taufiq, [ID] *[a] Arif Hidayat,[a] Erfan Handoko,[b] Mudrik Alaydrus,[c] Tahta Amrillah[d] and Itthipon Jeerapan [ID] [e]

Iron oxide/carbon-based nanocomposites are known as an ideal combination of magnetic–conductive materials that were recently developed in radar absorption application; one example is the Fe_3O_4/multiwalled carbon nanotubes (MWCNTs). In this study, we try to boost their radar absorption ability by Mn-ion doping. Mn is an appropriate Fe substitute that is predicted to alter the magnetic properties and enhance the conductivity, which are crucial to developing their radar absorption properties. Diethylamine (DEA) is also used as a capping agent to improve the size and shape of the nanocomposite. In this study, a $Mn_xFe_{3-x}O_4$–DEA/MWCNT nanocomposite is successfully prepared by the coprecipitation method using a variation of $x = 0$, 0.25, 0.5, 0.75, and 1. We found that the sample's magnetic saturation (M_s) decreases, while the reflection loss (RL) increases with increasing the molar fraction of Mn. The enhancement of the radar wave absorption in the sample is dominated by dielectric losses due to the increase of electrical conductivity and interfacial polarization with the addition of Mn in the nanocomposites. We believe that our finding could shed light on the role of doping elements to develop the radar absorption properties, and further pave the way for the real implementation of iron oxides/graphene-based nanocomposite as radar-absorbing materials (RAMs).

1. Introduction

Recently, the escalating growth of communication technology, particularly wireless communication, has led to a significant rise in electromagnetic pollution, emerging as a critical concern.[1] Electromagnetic pollution damages electronic devices, and has a detrimental effect on human health.[2,3] Therefore, researchers are currently working on the development of microwave-absorbing materials, particularly radar-absorbing materials (RAMs). Apart from addressing the issue of electromagnetic pollution, RAMs have potential applications in the military sector to conceal military defense equipment, such as fighter planes and tanks, from adversaries.[4] RAMs

attenuate the energy of electromagnetic waves by converting the waves into heat energy through magnetic and dielectric losses. Nevertheless, the primary challenge in RAM design lies in the selection of materials. To maximize their capability to absorb electromagnetic waves, a better understanding of how to engineer materials composed of magnetic and dielectric elements is required.

Fe_3O_4 nanoparticles (NPs) have garnered attention as potential microwave absorbents[5,6] owing to their unique features, including outstanding magnetic properties,[7,8] great permeability, excellent chemical and thermal stability,[9] high biocompatibility, and nontoxicity.[10] Despite these superiorities, Fe_3O_4 still has relatively low absorption[8] and deficient dielectric properties. Fe_3O_4 also tends to agglomerate;[11] therefore, the use of capping agents, such as PEG and PVP, as templates is essential.[12–14] However, they fail to generate NPs with uniform size and shape. Diethylamine (DEA) is one of the capping agents serving as a soft template for improving the size and shape of NPs to minimize agglomeration, which is also important to boost the absorption ability.[15,16]

The performance of Fe_3O_4 NPs in radar absorption can be improved through compositing and substitution with other materials. Recently, carbon nanotubes (CNTs) have gained attention as composite materials with Fe_3O_4 NPs owing to their

[a]Department of Physics, Faculty of Mathematics and Natural Science, State University of Malang, Jl. Semarang 5, Malang, 65145, Indonesia. E-mail: ahmad.taufiq.fmipa@um.ac.id

[b]Department of Physics, Faculty of Mathematics and Natural Sciences, Universitas Negeri Jakarta, Jl. Rawamangun Muka 1, Jakarta 13220, Indonesia

[c]Department of Electrical Engineering, Universitas Mercu Buana, Jl. Meruya Selatan 1, Jakarta 11650, Indonesia

[d]Nanotechnology Engineering, Faculty of Advanced Technology and Multidiscipline, Universitas Airlangga, Jl. Ir. Sukarno 1, Surabaya 60115, Indonesia

[e]Division of Physical Science, Faculty of Science, Prince of Songkla University, Hat Yai, Songkhla 90110, Thailand

dielectric, mechanical, electrical, and thermal properties and extensive surface area.[17] Multiwalled CNTs (MWCNTs) are one of the CNTs commonly composited with Fe_3O_4 NPs for numerous applications, including RAMs.[18] A combination of carbon and magnetic materials is considered as an effective strategy to obtain high-performance RAMs.[19] For RAM application, MWCNT offers excellent conductivity.[20] Combining MWCNT with Fe_3O_4 enhances the absorbing intensity and bandwidth and reduces RAM density, which benefits the performance of the RAM.[21] Fe_3O_4 as a magnetic component also could enrich the electromagnetic wave dissipation mechanism, which is important in wave absorption ability.[22] Nevertheless, although the iron oxides/graphene-based nanocomposite is known as an ideal combination of magnetic–conducting materials that was recently developed in radar absorption applications, further development is required. Various attempts had been carried out, such as element/ion substitution, shape or morphology modification, and compositing strategies. Among them, we believe that element/ion substitution could substantially develop the RAM. Thus, an in-depth exploration of this strategy is very important.

In this study, we performed Mn^{2+} ion substitution to improve the radar absorption ability and performance of Fe_3O_4–DEA/MWCNT. Mn^{2+} ion substitution can alter the magnetic properties of iron oxides since it has the appropriate atomic radii with Fe.[23] Magnetic properties are one of the vital parameters for Fe_3O_4 NP application in radar absorption application.[24] Mn ion substitution can also increase the conductivity of a material, including Fe_3O_4, which affects the dielectric loss of the RAM.[23,24] This study aims to identify the effects of Mn^{2+} ion substitution on the structure, morphology, and magnetic properties of Fe_3O_4–DEA/MWCNT nanocomposites. An in-depth study of the effect of Mn substitution is very important to pave the way for the real implementation of Fe_3O_4–DEA/MWCNT and other types of iron oxides/graphene-based nanocomposites as RAMs.

2. Experimental method

2.1. Synthesis of $Mn_xFe_{3-x}O_4$–DEA/MWCNT nanocomposites

Iron sand was used as the central precursor in the $Mn_xFe_{3-x}O_4$ preparation. $MnCl_2 \cdot 6H_2O$, DEA, HCl (12 M, 99.9%), NH_4OH (6.5 M, 999%), and HNO_3 (37%) were purchased from Merck. MWCNTs were obtained from Sigma-Aldrich, and distilled water was acquired from Pro Analysis. MWCNTs were functionalized as previously described.[25] First, 1 g of MWCNTs was mixed with 100 mL of HNO_3, and sonicated for 2 h at 40 kHz and 50 °C. The solution was filtered, washed using distilled water until pH 7, and then dried in an oven at 100 °C for 5 h to produce functionalized MWCNT powder (F-MWCNT). The synthesis of nanocomposites began with the production of $Mn_xFe_{3-x}O_4$. First, iron sand was separated using a permanent magnet to select the magnetic powder with high purity.[26] Then, 20 g of magnetic powder was reacted with 58 mL of HCl, followed by stirring for 30 min at room temperature to produce $FeCl_2$ and $FeCl_3$ solutions. $MnCl_2 \cdot 6H_2O$ with Mn_x fraction

variations of $x = 0, 0.25, 0.5, 0.75, 1$ was then added. We controlled the amount of molar fraction x with the calculated Mol divided with Mr, and reaction of $Mn_xFe_{3-x}O_4$ followed eqn (1).

$$xMn^{2+} + (1-x)Fe^{2+} + 2Fe^{3+} + 8OH^- \rightarrow Mn_xFe_{3-x}O_4 + 4H_2O \quad (1)$$
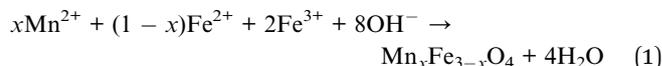
The solution was then mixed for 20 min, and titrated with 6 mL of DEA solution previously dissolved into 9 mL of distilled water. The titration products were combined with 0.1 g of F-MWCNT while stirring at room temperature. A total of 19 mL of NH_4OH was titrated until a black precipitate was obtained. The precipitate was washed using distilled water until pH 7, and then dried at 100 °C to attain a sample of the $Mn_xFe_{3-x}O_4$–DEA/MWCNT powder.

2.2. Characterizations

The structure, phase, crystallite size, and lattice parameter of the $Mn_xFe_{3-x}O_4$–DEA/MWCNT nanocomposites were investigated by X-ray diffraction (XRD) using X'Pert Pro test, Cu-Kα 1.540 Å Panalytical Merck with Cu-Kα 1.54060 Å radiation beam. The morphology and components of the nanocomposites were determined by scanning electron microscopy (SEM) combination of carb characterization type FEI, Inspect-S50. The functional groups within the sample were investigated using Fourier transform infrared (FTIR) spectroscopy type IRPrestige-21. The magnetic properties of the nanocomposites were characterized using a vibrating sample magnetometer (VSM) type PPMS VersaLab with a magnetic field ranging from −3 to 3 Tesla. Lastly, the radar absorption performance of the nanocomposites was characterized using vector network analyzer (VNA) type Rohde-Schwarz ZVA 67 to determine the complex permittivity, complex permeability, and reflection loss (RL).
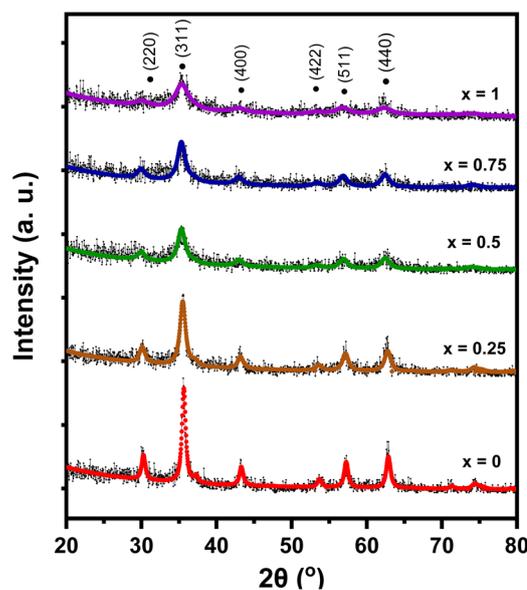

Fig. 1 Diffraction pattern of $Mn_xFe_{3-x}O_4$–DEA/MWCNT with different compositions of Mn substitution.

3.   Results and discussion

The XRD pattern of $Mn_xFe_{3-x}O_4$–DEA/MWCNT is presented in Fig. 1. Diffraction peaks with $x = 0$ code (Fig. 1) were detected at $2\theta = 30.21°$, $35.57°$, $43.13°$, $53.65°$, $57.13°$, and $62.69°$. This diffraction pattern is similar to that reported for Fe_3O_4–DEA.[15] The absence of new peaks following DEA addition suggests the successful utilization of DEA as a surfactant.[16] Furthermore, the lack of MWCNT diffraction peaks at $2\theta = 26°$ is caused by the lower mass of MWCNT relative to that of $Mn_xFe_{3-x}O_4$ at a ratio of 1 : 30 for MWCNT : $Mn_xFe_{3-x}O_4$. The diffraction patterns of all samples also indicate that the addition of Mn as a dopant ($x = 0.25–1$) generates the same pattern as that of the $x = 0$ sample. Therefore, our results showed that Mn addition causes no new peak or phase, signifying that Mn has successfully penetrated Fe_3O_4. Li et $al.$ demonstrated that the absence of new peaks on $Mn_xFe_{3-x}O_4$ indicates that Mn^{2+} successfully enters $Mn_xFe_{3-x}O_4$, replaces Fe^{3+}, and does not form MnO_2 deposits on the Fe_3O_4 surface.[27]

We performed a quantitative analysis by comparing the obtained data with the ICSD database number 30860. The results showed that the observed peaks are identical with the Miller index of (220), (311), (400), (422), (511), and (440), with the highest peak observed at $\sim 2\theta = 35.5°$ on the hkl (311). This finding indicates the single phase of the sample with cubic spinel structure and the space group of $Fd3m$. The diffraction patterns at hkl (220) and (311) demonstrate a shift towards smaller 2θ values with Mn substitution. This shift is associated with the increase in the sample's lattice parameters (8.361–8.429 Å) due to Mn substitution, as summarized in Table 1. The observed increase in lattice parameter is attributed to the effects of ionic size because Mn^{2+} (0.81 Å) possesses a larger ionic radius compared to Fe^{3+} (0.77 Å).[28] Therefore, Mn substitution on Fe_3O_4 drives the expansion of cell units, as proven by the expanded sample's crystal volume shown in Table 1 and Fig. 2. This finding also signifies that some Fe^{3+} ions on the tetrahedral structure have been substituted by Mn^{2+} ions.[24] Our results are similar to those of a previous study reporting an increase in lattice parameters from 8.372 Å to 8.474 Å with Mn^{2+} substitution on $x = 0.25$ to $x = 1$ variations.[29]

Table 1 Crystallite size, lattice parameter, and crystal volume of $Mn_xFe_{3-x}O_4$–DEA/MWCNT

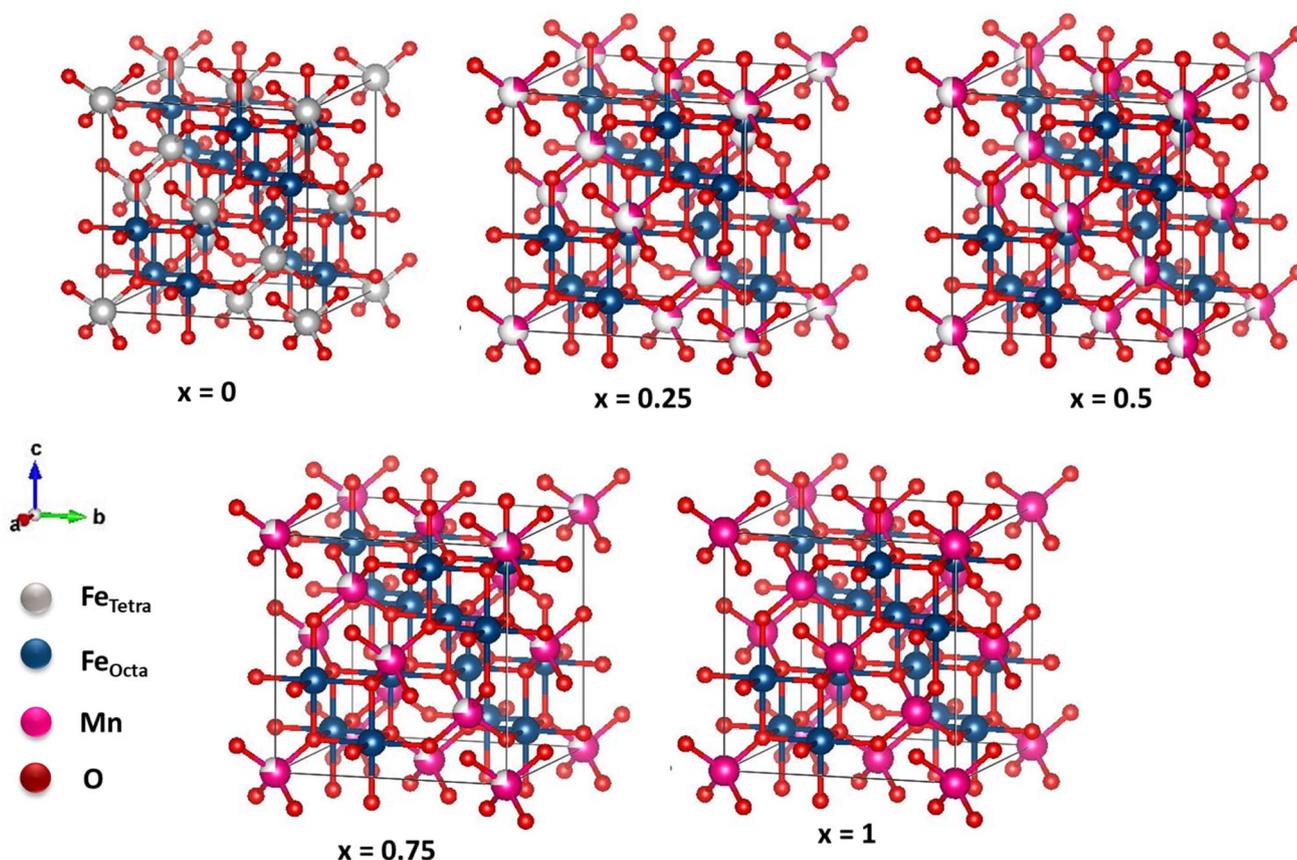| Samples	Crystallite size (nm)	Lattice parameter (Å)	Crystal volume (Å³)
$x = 0$	17.0 ± 0.2	8.361 ± 0.003	584.5 ± 0.3
$x = 0.25$	11.0 ± 0.3	8.385 ± 0.001	589.5 ± 0.2
$x = 0.5$	8.0 ± 0.1	8.404 ± 0.003	593.6 ± 0.1
$x = 0.75$	7.9 ± 0.2	8.409 ± 0.002	594.6 ± 0.2
$x = 1$	4.5 ± 0.3	8.419 ± 0.002	596.7 ± 0.5

Fig. 2 Possible crystal structure of $Mn_xFe_{3-x}O_4$ with different compositions of Mn substitution.

The crystal structure of $Mn_xFe_{3-x}O_4$ is illustrated in Fig. 2. The $x = 0$ sample structure has an inverse cubic spinel structure with eight Fe^{3+} ions in the tetrahedral site, and eight Fe^{2+} and Fe^{3+} ions in the octahedral site. The addition of Mn^{2+} has enlarged the cubic spinel crystal structure compared to that of the sample $x = 0$, signifying the expansion of the cell unit. In samples with $x = 0.25$, 0.5, and 0.75, Mn^{2+} ions replace some Fe^{3+} ions on the tetrahedral site. In sample $x = 1$, all Fe^{3+} ions are substituted by Mn^{2+} ions. Four and six O ions are observed surrounding the Fe^{2+}, Fe^{3+}, and Mn^{2+} ions on the tetrahedral and octahedral sites, respectively.

Fig. 3 displays the graph depicting variations in the lattice parameters and Mn molar fraction variations. The Mn molar fraction demonstrates an increasing trend with two distinct slopes: one for molar fractions ranging from 0 to 0.5, and another for molar fractions from 0.5 to 1. This observed trend closely resembles the increase in lattice parameters reported in a previous study of about ~ 8.4 Å.[30] Additionally, this trend is consistent with the Mössbauer results, which indicate that Mn^{2+} ions replace Fe^{3+} ions on the tetrahedral sites. This finding is supported by the Mössbauer spectroscopy, which shows that the iron ions on the $MnFe_2O_4$ system are in the 3+ state, allowing the substitution of Mn^{2+} to be written as $(Fe_{x-1}{}^{2+}Fe_{x+1}{}^{3+})_{octa}(Mn_x{}^{2+}Fe_{x-1}{}^{3+})_{tetra}$.

The crystallite size of the $Mn_xFe_{3-x}O_4$–DEA/MWCNT nanocomposites decreases with the increase in Mn substitution, which is consistent with previous results.[23] The reduced crystallite size is caused by the addition of DEA as the controlling and reducing agent for the crystallite size. Taufiq *et al.* similarly reported that all synthesized Fe_3O_4 samples with the DEA template present a nanometric particle size, which decreases upon the addition of DEA at high concentrations.[16] By using DEA, the particle size of the nanocomposite is easy to control. Thus, by controlling the particle size, we also can tune the absorbance ability of the nanocomposite.[19]

The morphology of the $Mn_xFe_{3-x}O_4$–DEA/MWCNT nanocomposites was assessed by SEM characterization. The SEM

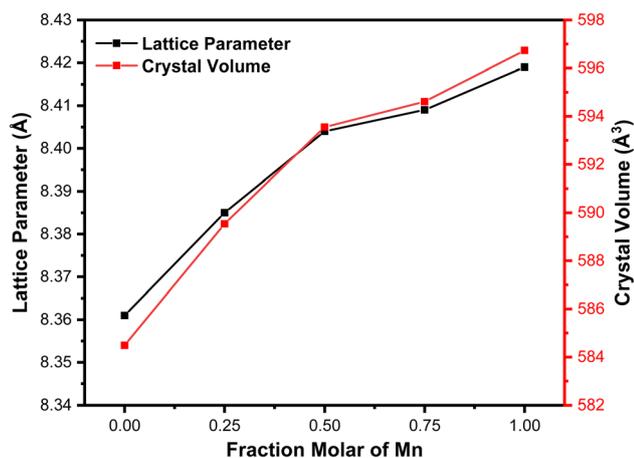**Fig. 3** Relationship of the Mn molar fraction (x) with the lattice parameter and crystal volume.
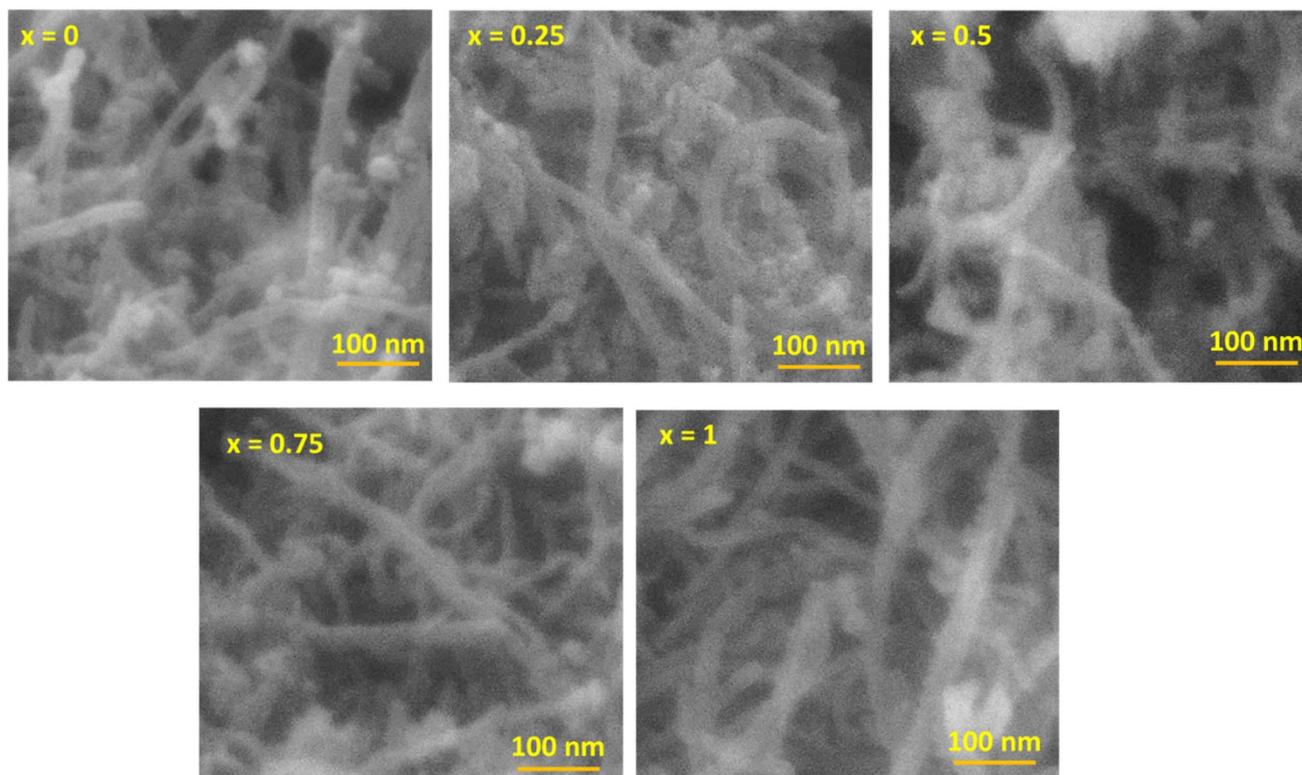

Fig. 4 Morphology of $Mn_xFe_{3-x}O_4$–DEA/MWCNT with $x = 0.25$–1 at $100\,000\times$ magnification.

image with $100\,000\times$ magnification is presented in Fig. 4. The $Mn_xFe_{3-x}O_4$ cluster is in the form of a chunk, and the MWCNTs exhibit a cylindrical shape. The MWCNTs in the cylinder form a shroud and bind to the spherical $Mn_xFe_{3-x}O_4$ chunk. The bond arises due to MWCNT functionalization, which introduces OH-functional groups on the MWCNT surface. These groups interact with the positive charge of $Mn_xFe_{3-x}O_4$, as depicted in Fig. 5. Theoretically, the positive ions of Fe_3O_4, such as Mn^{2+}, Fe^{2+}, or Fe^{3+}, form bonds with the negative ions and the charged carboxyl group on the MWCNT surface, facilitated by the MWCNT functionalization using HNO_3. The presence of the carboxyl group and damage in certain parts of MWCNT facilitates its binding to other compounds, in this case, $Mn_xFe_{3-x}O_4$–DEA.[18]

The carboxyl group with a negative charge will interact with $Mn_xFe_{3-x}O_4$ having positive ions (Mn^{2+}, Fe^{2+}, and Fe^{3+}), which initiate an electrostatic attraction and increase the structural stability of the nanocomposites.[31,32] Due to this fact, $Mn_xFe_{3-x}O_4$ is strongly bonded to the surface of MWCNT. MWCNT also serves as a barrier to suppress the aggregation tendency of $Mn_xFe_{3-x}O_4$, and thus further increases the structural stability.[33] In addition, the morphology of MWCNTs that form a long tube shape tends to have better conductivity because they can form a more continuous conductive path. This agrees with previous reports indicating that RAMs with tubular shape and considerable anisotropy can form three-dimensional conduction networks to enhance its conductivity.[34] This condition favors wave propagation through the material and its attenuation. Thus, an excellent wave attenuation in this proposed RAM could be induced due to the excellent interface between CNTs and $Mn_xFe_{3-x}O_4$, which creates an interface polarization.[35] It is important to note that the interface polarization could induce excellent dielectric loss capacity for microwave absorption of the nanocomposite.[34] Controlling the shapes and morphology of RAMs is important because the microwave absorption ability

also depends on the degree of density, weight and dispersion of RAMs itself.[36] The morphology of the nanocomposites after Mn addition, as depicted in Fig. 4, closely resembles the nanocomposites with a molar fraction of 0. Moreover, we observed a decrease in agglomeration with Mn addition. On the other hand, the further reduction of agglomeration upon inclusion of DEA was also indicated.[18,37]

Fig. 6 shows the FTIR spectrum of the $Mn_xFe_{3-x}O_4$ nanocomposites. At 3491–3290 cm^{-1}, we identified a widened O–H vibration, possibly induced by the –OH groups on the surface areas. This functional group facilitates the combination of Mn–Fe_2O_4 with MWCNT.[15,38] Our obtained vibrations are similar to the vibrational peak of O–H reported in previous studies, specifically those at 3321,[25] 3420,[38] and 3430 cm^{-1}.[15] We also detected the C–O functional groups at 2325 and

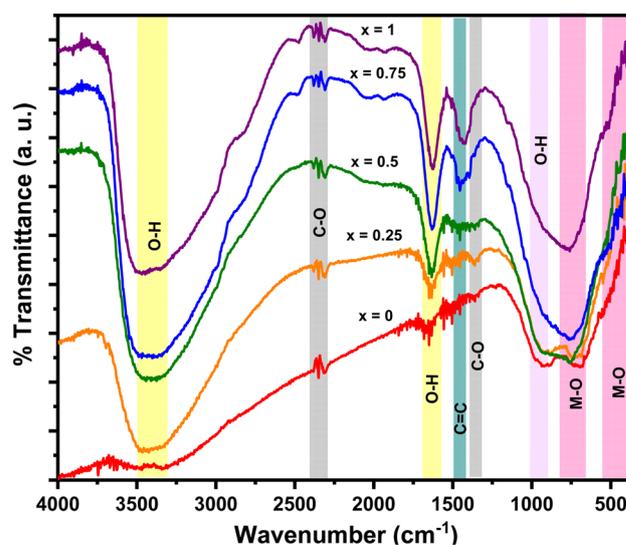**Fig. 6** FTIR spectrum for the $Mn_xFe_{3-x}O_4$–DEA/MWCNT nanocomposites with different compositions of Mn substitution.
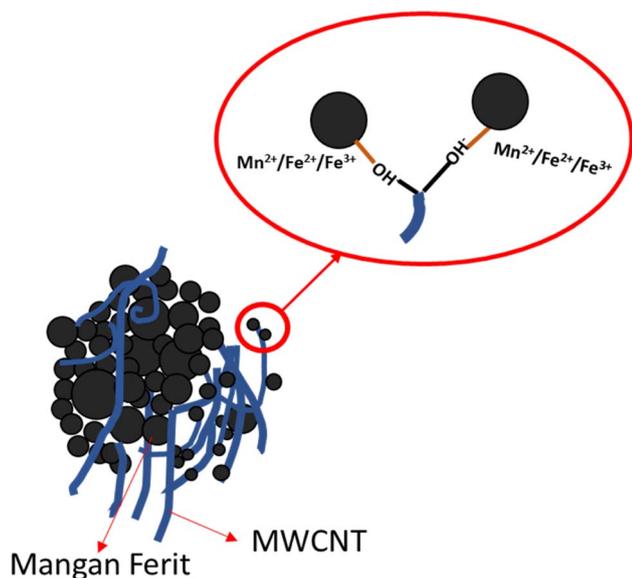

Fig. 5 The illustration of $Mn_xFe_{3-x}O_4$–DEA/MWCNT with $x = 0.25$–1.

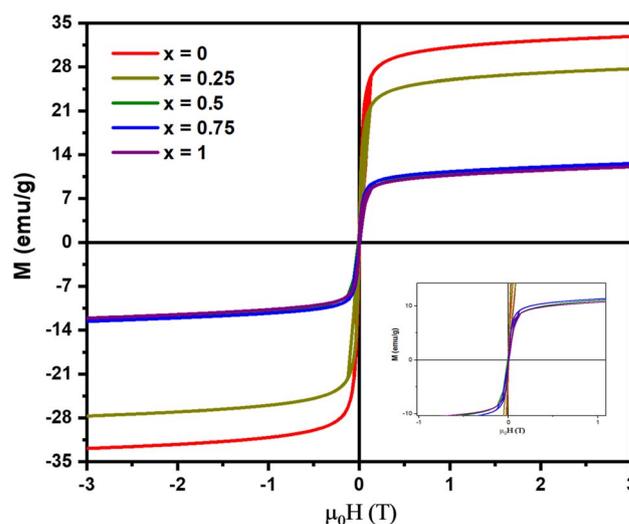**Fig. 7** M–H hysteresis curves of the $Mn_xFe_{3-x}O_4$–DEA/MWCNT nanocomposites.
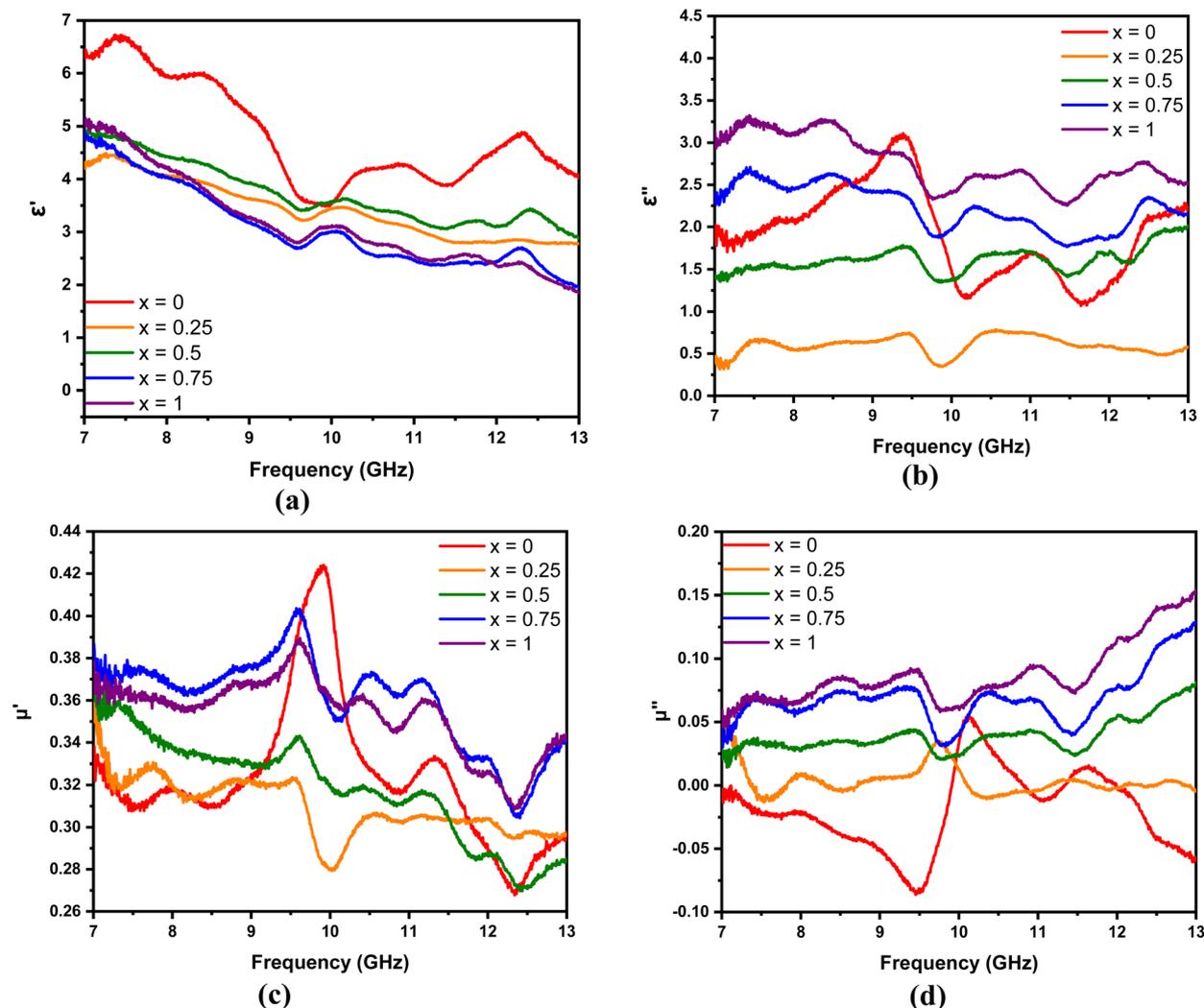
1359 cm^{-1} that are possibly from the CO_2 atmosphere[15] and identified the C=C functional group at 1438 cm^{-1}, characterizing the graphite bonds compiled in the MWCNT. No functional groups of DEA are found, especially N–H, C–N, and N–H at 733, 1143, and 3288 cm^{-1}, respectively. This finding suggests that the DEA used in nanoparticle preparation has not evaporated. The functional groups of metal oxide (M–O), namely, Fe–O and Mn–O, are detected at 412 and 673 cm^{-1}. These two vibrations indicate that the manganese ferrite has a cubic spinel structure at the octahedral and tetrahedral sites. This finding is in line with a previous study reporting vibration peaks in the range of 430–482 cm^{-1} and 433–573 cm^{-1}.[39] As illustrated in Fig. 6, the absorbance intensity between 600 and 700 cm^{-1} increases with further addition of Mn molar fraction. This finding confirms the success of the Mn^{2+} ions in substituting Fe^{3+} ions in the tetrahedral sites. In addition, the increasing concentration of Mn leads to a shift of absorbance peaks towards lower wavenumbers. This phenomenon is correlated with the increase in the distance between two atoms, which occurs due to the increase in lattice parameters.

Fig. 7 shows the M–H hysteresis curve from the VSM analysis of the $Mn_xFe_{3-x}O_4$–DEA/MWCNT nanocomposites. All samples show superparamagnetic features as indicated by the obtained S curve. The attained hysteresis curve was then analyzed using the Langevin method with susceptibility,[40] and the results are summarized in Table 2. The remanent magnetization and coercivity field are close to 0, characterizing the superparamagnetic

Table 2 Magnetization saturation, remanent magnetization, coercivity field, and susceptibility of the $Mn_xFe_{3-x}O_4$–DEA/MWCNT

Samples	M_s (emu g^{-1})	M_r (emu g^{-1})	H_c (T)	χ
$x = 0$	32.32 ± 0.03	-0.013 ± 0.012	0.520 ± 0.001	0.81 ± 0.02
$x = 0.25$	27.12 ± 0.03	-0.012 ± 0.011	0.510 ± 0.003	0.84 ± 0.02
$x = 0.5$	12.07 ± 0.02	-0.010 ± 0.002	0.066 ± 0.015	0.65 ± 0.01
$x = 0.75$	11.91 ± 0.02	-0.005 ± 0.001	0.052 ± 0.001	0.78 ± 0.01
$x = 1$	11.51 ± 0.02	-0.011 ± 0.004	0.010 ± 0.002	0.71 ± 0.01

Fig. 8 (a)–(c) Real and (b)–(d) imaginary parts of the permittivity and permeability of $Mn_xFe_{3-x}O_4$–DEA/MWCNT with different compositions of Mn substitution, respectively.

components.[30] The highest magnetization of 32.32 ± 0.03 emu g^{-1} is observed for $Mn_xFe_{3-x}O_4$–DEA/MWCNT at $x = 0$. This value is lower than the previously reported magnetization of Fe_3O_4–DEA at 35.76 emu g^{-1}. Therefore, the obtained values can be correlated with the addition of MWCNT (nonmagnetic), *i.e.*, MWCNT lowers the magnetic fraction of the samples and affects the M_s value. In our previous study, we uncovered that Fe_3O_4/MWCNT has M_s of 12.64 and 21.15 emu g^{-1}, which are lower than the magnetization values obtained in the present work. The addition of DEA to the nanocomposites also affects the sample's magnetization. The magnetization values also decrease following the increase in the Mn molar fraction substituted for Fe_3O_4. This decrease can also be attributed to the low crystallite value, as demonstrated in Table 1. Nanosized particles typically have a single domain and exhibit paramagnetic behavior, resulting in an increased spin disorder on the nanoparticle's surface, which subsequently reduces the magnetic moment.[41]

The real and imaginary parameters of the electrical permittivity (real permittivity (ε') and imaginary permittivity (ε'')) and the magnetic permeability (real permeability (μ') and imaginary permeability (μ'')) shown in Fig. 8 are parameters used to determine the absorption mechanism of the $Mn_xFe_{3-x}O_4$–DEA/MWCNT nanocomposites for radar waves. ε' and μ' represent the ability to store electric and magnetic energy, respectively; and ε'' and μ'' are related to the dissipation and loss of electric and magnetic energy, respectively. As illustrated in Fig. 8(a), which is the ε' curve, the real permittivity value decreases from 6.4 to 4.2 when the molar fraction of Mn increases. Meanwhile, the ε'' value tends to be greater after Mn addition, which can be explained by eqn (2).

$$\varepsilon'' = \varepsilon''_p + \varepsilon''_c = \varepsilon_s - \varepsilon_\infty$$

$$\frac{2\pi f \tau}{1 + (2\pi f)^2} + \frac{\sigma}{2\pi f \varepsilon_0} = \frac{\varepsilon_s - \varepsilon_\infty}{1 + \omega^2\tau^2}\omega\tau + \frac{\sigma}{\omega\varepsilon_0} \quad (2)$$

According to eqn (2), an increase in ε'' is related to electrical conductivity. Mn substitution increases the conductivity value of a material due to the production of holes during charge
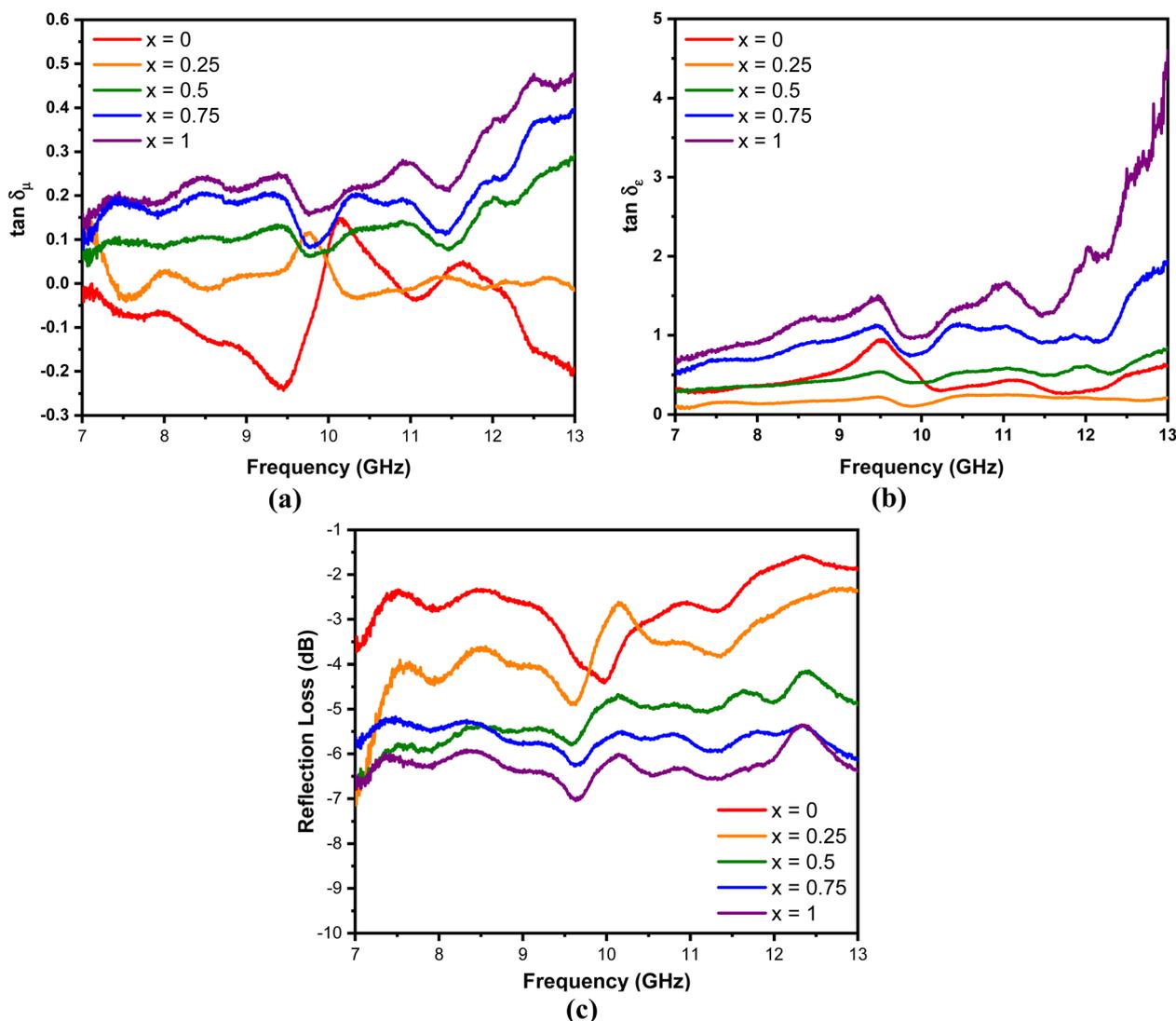

Fig. 9 (a) tan δ_μ, (b) tan δ_ε, and (c) RL of $Mn_xFe_{3-x}O_4$–DEA/MWCNT with different compositions of Mn substitution.

transfer.[42] An increase in electrical conductivity also increases the loss and dissipation ability of the electric part, as indicated by the ε'' value of the nanocomposites with $x = 1$ greater than $x = 0$. In addition to electrical conductivity, the ε'' value is related to interfacial polarization, which is marked by several resonance peaks around the frequencies of 7.5, 8.5, 9.5, 11, and 12.5 GHz. These peaks are related to the relaxation stage when interfacial polarization occurs.[2]

The μ' and μ'' of $Mn_xFe_{3-x}O_4$–DEA/MWCNT are shown in Fig. 8(c) and (d), respectively. The μ' of all samples tends to decrease gradually, and the μ'' increases with the frequency. Fluctuations are observed in the μ' and μ'' curves, especially at frequencies above 9 GHz. The fluctuation peaks represent the resonance peaks, where the absorbance peaks at low frequencies originate from the wall resonance domain, and the peaks at high frequencies correspond to natural resonance. Furthermore, the μ'' of the sample with Mn addition is greater than that of the sample without Mn substitution. This finding indicates that the magnetic loss of the nanocomposites increases with the molar fraction of Mn. The μ'' in the sample $x = 0$ shows a negative value at several frequencies, implying that the magnetic energy from this sample is directly emitted without being absorbed at that frequency.[43]

$$\tan \delta_\mu = \frac{\mu''}{\mu'} \tag{3}$$

$$\tan \delta_\varepsilon = \frac{\varepsilon''}{\varepsilon'} \tag{4}$$

In general, the absorption capability of radar waves is described by magnetic loss and dielectric loss, which are represented by $\tan \delta_\mu$ and $\tan \delta_\varepsilon$, respectively. $\tan \delta_\mu$ and $\tan \delta_\varepsilon$ describe the loss capacity of the radar absorption materials, and can be calculated using eqn (3) and (4), respectively. Fig. 9 shows the relationship of $\tan \delta_\mu$ and $\tan \delta_\varepsilon$ with frequency. Comparison between Fig. 9(a) and (b) shows that the $\tan \delta_\varepsilon$ value is higher than the $\tan \delta_\mu$ value. These results explain that dielectric loss is the main contributor to the absorption of radar waves by the $Mn_xFe_{3-x}O_4$–DEA/MWCNT nanocomposites.[44]

The performance of the $Mn_xFe_{3-x}O_4$–DEA/MWCNT nanocomposites for the absorption of radar waves is shown as a graph of the relationship between the reflection loss (RL) and frequency depicted in Fig. 9(c). The RL values of $Mn_xFe_{3-x}O_4$–DEA/MWCNT for $x = 0$–1 are −4.39, −4.85, −5.77, −6.26, and −7.03 dB. The increase in RL is associated with a decrease in particle size as the molar fraction of Mn increases in the nanocomposites. Nanocomposites with a small size have a large proportion of surface atoms, which can be magnetized and polarized under an external electromagnetic field. This situation allows the radar wave energy to be converted into heat, resulting in high RL values.[45] The highest RL of −7.03 dB is recorded for the sample with $x = 1$, which is consistent with the highest $\tan \delta_\mu$ and $\tan \delta_\varepsilon$ values (magnetic and dielectric loss) for this sample. In addition, $x = 1$ has a smaller crystallite size than other samples (Table 1). A low particle size is associated with a high dipole polarization that induces dielectric loss.[46] In addition, the particle sizes also affect the degree of density, weight, and dispersion of nanocomposites, which further affect their absorption ability.[36]

4. Conclusion

$Mn_xFe_{3-x}O_4$–DEA/MWCNT nanocomposites have been successfully synthesized by the coprecipitation method having Mn fraction variations of $x = 0$, 0.25, 0.5, 0.75, 1. The crystallite size decreases from 17 to 4.5 nm with the increase in substituted Mn substitution. The morphology of the nanocomposites contains spherical shapes and chunks of $Mn_xFe_{3-x}O_4$, as well as tubular shapes of the MWCNT, indicating they are physically contacted. All of the synthesized nanocomposites exhibit superparamagnetism with the tendency of decreasing saturation magnetization at around 32.32 ± 0.03 to 11.51 ± 0.02 emu g^{-1} due to Mn addition, which presumably enhances the spin disorder on the nanocomposite's surface. Furthermore, the performance of the nanocomposites in absorbing radar waves is shown by the RL value that increases from −4.39 to −7.03 dB with the increase in the molar fraction of Mn. It shows that the radar absorption performance of the $Mn_xFe_{3-x}O_4$–DEA/MWCNT nanocomposites is dominated by dielectric loss, owing to increased electrical conductivity and interfacial polarization with the addition of Mn. We believe that our findings may shed light on the role of substitution elements in developing the radar absorption properties not only for $Mn_xFe_{3-x}O_4$–DEA/MWCNT nanocomposites, but also for other iron oxides/graphene-based nanocomposites, which further pave the way for their real implementation as RAMs.

Conflicts of interest

There are no conflicts to declare.

Acknowledgements

References

1 H. Yao, J. Yang, H. Li, J. Xu and K. Bi, Optimal design of multilayer radar absorbing materials: a simulation-optimization approach, *Adv. Compos. Hybrid Mater.*, 2023, **6**(1), 43, DOI: **10.1007/s42114-023-00626-3**.

2 M. M. A. Yahya, *et al.*, Investigation of the optical, magnetic, and radar absorption characteristics of $Co_xFe_{3-x}O_4$/ZnO/graphite nanocomposites, *Mater. Sci. Semicond. Process.*, 2023, **165**, 107683, DOI: **10.1016/j.mssp.2023.107683**.

3 F. Meng, *et al.*, Graphene-based microwave absorbing composites: a review and prospective, *Composites, Part B*, 2018, **137**, 260–277, DOI: **10.1016/j.compositesb.2017.11.023**.

4 P. Sahoo, L. Saini and A. Dixit, Microwave-absorbing materials for stealth application: a holistic overview, *Oxf. Open Mater. Sci.*, 2023, **3**(1), itac012, DOI: **10.1093/oxfmat/itac012**.

5 Y. Xie, *et al.*, Efficient electromagnetic wave absorption performances dominated by exchanged resonance of lightweight PC/Fe$_3$O$_4$@PDA hybrid nanocomposite, *Chem. Eng. J.*, 2023, **457**, 141205, DOI: **10.1016/j.cej.2022.141205**.

6 W. Xia, X. Wang, D. Liu, C. Li, J. Xie and C. Xiong, Enhanced microwave absorbing performance of epoxy composites filled with solvent-free and liquid-like Fe$_3$O$_4$ organic hybrid material, *Appl. Surf. Sci.*, 2023, **615**, 156376, DOI: **10.1016/j.apsusc.2023.156376**.

7 S. Wei, R. Yan, B. Shi and X. Chen, Characterization of flexible radar-absorbing materials based on ferromagnetic nickel micron-fibers, *J. Ind. Text.*, 2019, **49**(1), 58–70, DOI: **10.1177/1528083718772304**.

8 A. Taufiq, *et al.*, Radar Absorption Performance of Fe$_3$O$_4$/AC/PANI Nanocomposites Prepared from Natural Iron Sand, *Int. J. Eng.*, 2020, **33**(2), 2.

9 E. Bagheripour, A. Moghadassi and S. M. Hosseini, Incorporated poly acrylic acid-co- Fe$_3$O$_4$ nanoparticles mixed matrix polyethersulfone based nanofiltration membrane in desalination process, *Int. J. Eng.*, 2017, **30**(6), 821–829.

10 X.-H. Do, *et al.*, High Biocompatibility, MRI Enhancement, and Dual Chemo- and Thermal-Therapy of Curcumin-Encapsulated Alginate/Fe$_3$O$_4$ Nanoparticles, *Pharmaceutics*, 2023, **15**(5), 5, DOI: **10.3390/pharmaceutics15051523**.

11 L. Maldonado-Camargo, I. Torres-Díaz, A. Chiu-Lam, M. Hernández and C. Rinaldi, Estimating the contribution of Brownian and Néel relaxation in a magnetic fluid through dynamic magnetic susceptibility measurements, *J. Magn. Magn. Mater.*, 2016, **412**, 223–233, DOI: **10.1016/j.jmmm.2016.03.087**.

12 D. Arista, A. Rachmawati, N. Ramadhani, R. E. Saputro and A. Taufiq, Antibacterial performance of Fe$_3$O$_4$/PEG-4000 prepared by co-precipitation route, *IOP Conf. Ser.: Mater. Sci. Eng.*, 2019, 012085.

13 M. S. Jabir, U. M. Nayef, W. K. Abdulkadhim and G. M. Sulaiman, Supermagnetic Fe$_3$O$_4$-PEG nanoparticles combined with NIR laser and alternating magnetic field as potent anti-cancer agent against human ovarian cancer cells, *Mater. Res. Express*, 2019, **6**(11), 115412, DOI: **10.1088/2053-1591/ab50a0**.

14 X. Wang, F. Pan, Z. Xiang, W. Jia and W. Lu, Magnetic Fe$_3$O$_4$@PVP nanotubes with high heating efficiency for MRI-guided magnetic hyperthermia applications, *Mater. Lett.*, 2020, **262**, 127187, DOI: **10.1016/j.matlet.2019.127187**.

15 A. Taufiq, *et al.*, Preparation of Superparamagnetic Fe$_3$O$_4$ Nanoparticles from Iron Sand Mediated by Soft Template and Their Performance as Antibacterial Agent, *J. Magn.*, 2018, **23**(3), 3, DOI: **10.4283/JMAG.2018.23.3.337**.

16 S. U. I. Subadra, *et al.*, Synthesis and characterisation of Fe$_3$O$_4$/MWCNT/ZnO nanocomposites covered by a soft template as a new antibacterial agent, *Adv. Nat. Sci.: Nanosci. Nanotechnol.*, 2022, **13**(3), 035010, DOI: **10.1088/2043-6262/ac8de8**.

17 E. Sano and E. Akiba, Electromagnetic absorbing materials using nonwoven fabrics coated with multi-walled carbon nanotubes, *Carbon*, 2014, **78**, 463–468, DOI: **10.1016/j.carbon.2014.07.027**.

18 A. Taufiq, *et al.*, Eco-Friendly Fabrication of Fe$_3$O$_4$/MWCNT/ZnO Nanocomposites from Natural Sand for Radar Absorbing Materials, *Int. J. Nanosci. Nanotechnol.*, 2021, **17**(1), 41–53.

19 T. Hou, J. Wang, T. Zheng, Y. Liu, G. Wu and P. Yin, Anion Exchange of Metal Particles on Carbon-Based Skeletons for Promoting Dielectric Equilibrium and High-Efficiency Electromagnetic Wave Absorption, *Small*, 2023, 2303463, DOI: **10.1002/smll.202303463**.

20 P. Saini, V. Choudhary, B. P. Singh, R. B. Mathur and S. K. Dhawan, Polyaniline–MWCNT nanocomposites for microwave absorption and EMI shielding, *Mater. Chem. Phys.*, 2009, **113**(2–3), 919–926, DOI: **10.1016/j.matchemphys.2008.08.065**.

21 F. Ruiz-Perez, S. M. López-Estrada, R. V. Tolentino-Hernández and F. Caballero-Briones, Carbon-based radar absorbing materials: a critical review, *J. Sci.: Adv. Mater. Devices*, 2022, **7**(3), 100454, DOI: **10.1016/j.jsamd.2022.100454**.

22 M. Chang, Z. Jia, G. Wu and P. Yin, Multiple dimension-component designed Co/Co$_9$S$_8$/Ti$_3$C$_2$T$_x$ MXene composite for enhanced microwave absorption, *Appl. Phys. Lett.*, 2023, **122**, 131901, DOI: **10.1063/5.0142497**.

23 A. Taufiq, *et al.*, Studies on Nanostructure and Magnetic Behaviors of Mn-Doped Black Iron Oxide Magnetic Fluids Synthesized from Iron Sand, *Nano*, 2017, **12**(09), 09, DOI: **10.1142/S1793292017501107**.

24 A. Taufiq, *et al.*, Nanoscale Clustering and Magnetic Properties of Mn$_x$Fe$_{3−x}$O$_4$ Particles Prepared from Natural Magnetite, *J. Supercond. Novel Magn.*, 2015, **28**(9), 2855–2863, DOI: **10.1007/s10948-015-3111-9**.

25 R. Rahmawati, *et al.*, Preparation of MWCNT-Fe$_3$O$_4$ Nanocomposites from Iron Sand Using Sonochemical Route, *IOP Conf. Ser.: Mater. Sci. Eng.*, 2017, **202**, 012013, DOI: **10.1088/1757-899X/202/1/012013**.

26 A. Taufiq, *et al.*, Fabrication of Mn$_{1-x}$Zn$_x$Fe$_2$O$_4$ ferrofluids from natural sand for magnetic sensors and radar absorbing materials, *Heliyon*, 2020, **6**(7), e04577.

27 M. Li, *et al.*, Solvothermal synthesis of Mn$_x$Fe$_{3−x}$O$_4$ nanoparticles with interesting physicochemical characteristics and good catalytic degradation activity, *Mater. Des.*, 2016, **97**, 341–348, DOI: **10.1016/j.matdes.2016.02.103**.

28 J. S. Anandhi, G. A. Jacob and R. J. Joseyphus, Factors affecting the heating efficiency of Mn-doped Fe$_3$O$_4$ nanoparticles, *J. Magn. Magn. Mater.*, 2020, **512**, 166992, DOI: **10.1016/j.jmmm.2020.166992**.

29 A. Doaga, *et al.*, Synthesis and characterizations of manganese ferrites for hyperthermia applications, *Mater. Chem. Phys.*, 2013, **143**(1), 305–310, DOI: **10.1016/j.matchemphys.2013.08.066**.

30 S. T. Yazdi, P. Iranmanesh, S. Saeednia and M. Mehran, Structural, optical and magnetic properties of Mn$_x$Fe$_{3−x}$O$_4$ nanoferrites synthesized by a simple capping agent-free

coprecipitation route, *Mater. Sci. Eng., B*, 2019, **245**, 55–62, DOI: **10.1016/j.mseb.2019.05.009**.

31 S.-D. Seo, G.-H. Lee and D.-W. Kim, Enhanced electroactivity with Li in Fe₃O₄/MWCNT nanocomposite electrodes, *J. Alloys Compd.*, 2014, **615**, S397–S400, DOI: **10.1016/j.jallcom.2014.01.077**.

32 Y. Huang, K. Yang and J.-Y. Dong, Copolymerization of Ethylene and 10-Undecen-1-ol using a Montmorillonite-Intercalated Metallocene Catalyst: Synthesis of Polyethylene/Montmorillonite Nanocomposites with Enhanced Structural Stability, *Macromol. Rapid Commun.*, 2006, **27**, 1278–1283, DOI: **10.1002/marc.200600131**.

33 J. Tang and J. Wang, Fe₃O₄-MWCNT Magnetic Nanocomposites as Efficient Fenton-Like Catalysts for Degradation of Sulfamethazine in Aqueous Solution, *ChemistrySelect*, 2017, **2**, 10727–10735, DOI: **10.1002/slct.201702249**.

34 P. Yin, G. Wu, Y. Tang, S. Liu, Y. Zhang, G. Bu, J. Dai, Y. Zhao and Y. Liu, Structure regulation in N-doping biconical carbon frame decorated with CoFe₂O₄ and (Fe,Ni) for broadband microwave absorption, *Chem. Eng. J.*, 2022, **446**, 136975, DOI: **10.1016/j.cej.2022.136975**.

35 V. A. Silva and M. C. Rezende, S-parameters, electrical permittivity, and absorbing energy measurements of carbon nanotubes-based composites in X-band, *J. Appl. Polym. Sci.*, 2021, **138**, 49843, DOI: **10.1002/app.49843**.

36 T. Zheng, Y. Zhang, Z. Jia, J. Zhu, G. Wu and P. Yin, Customized dielectric-magnetic balance enhanced electromagnetic wave absorption performance in Cu$_x$S/CoFe₂O₄ composites, *Chem. Eng. J.*, 2023, **457**, 140876, DOI: **10.1016/j.cej.2022.140876**.

37 R. Rameshbabu, R. Ramesh, S. Kanagesan, A. Karthigeyan and S. Ponnusamy, One pot facile hydrothermal synthesis of superparamagnetic ZnFe₂O₄ nanoparticles and their properties, *J. Sol-Gel Sci. Technol.*, 2014, **71**(1), 147–151, DOI: **10.1007/s10971-014-3347-z**.

38 Z. Chen, *et al.*, Magnetic Mn-Doped Fe₃O₄ hollow Microsphere/RGO heterogeneous Photo-Fenton Catalyst for high efficiency degradation of organic pollutant at neutral pH, *Mater. Chem. Phys.*, 2019, **238**, 121893, DOI: **10.1016/j.matchemphys.2019.121893**.

39 K. Saputra, *et al.*, Effect of Polyethylene Glycol (PEG) on Particle Distribution of Mn₀.₂₅Fe₂.₇₅O₄-PEG 6000 Nanoparticles, *J. Phys.: Conf. Ser.*, 2018, 012005.

40 A. Taufiq, S. N. Qoidah, S. U. I. Subadra, A. Mufti, A. Hidayat and Sunaryono, Preparation of Fe₃O₄/MWCNT nanocomposite combined with titanium dioxide using sonochemical and precipitation methods, *AIP Conf. Proc.*, 2020, 020007.

41 G. F. Goya, T. S. Berquo, F. C. Fonseca and M. P. Morales, Static and dynamic magnetic properties of spherical magnetite nanoparticles, *J. Appl. Phys.*, 2003, **94**(5), 3520–3528.

42 N. Helaïli, Y. Bessekhouad, K. Bachari and M. Trari, Synthesis and physical properties of the CuFe₂₋$_x$Mn$_x$O₄ (0 ≤ x ≤ 2) solid solution, *Mater. Chem. Phys.*, 2014, **148**(3), 734–743, DOI: **10.1016/j.matchemphys.2014.08.042**.

43 M. M. Ismail, S. N. Rafeeq, J. M. Sulaiman and A. Mandal, Electromagnetic interference shielding and microwave absorption properties of cobalt ferrite CoFe₂O₄/polyaniline composite, *Appl. Phys. A: Mater. Sci. Process.*, 2018, **124**, 1–12.

44 Y. Luo, P. Yin, G. Wu, L. Zhang, G. Ma, J. Wang, X. Sun and G. Bu, Porous carbon sphere decorated with Co/Ni nanoparticles for strong and broadband electromagnetic dissipation, *Carbon*, 2022, **197**, 389–399, DOI: **10.1016/j.carbon.2022.06.084**.

45 F. Jiang, X. Wei and J. Zheng, Synthesis and electromagnetic characteristics of MnFe₂O₄/TiO₂ composite material, *Mater. Res. Express*, 2022, **9**(10), 106101, DOI: **10.1088/2053-1591/ac97de**.

46 L. Ahmadian-Alam, F. Jahangiri and H. Mahdavi, Fabrication and assessment of an electrochromic and radar-absorbent dual device based on the new smart polythiophene-based/RGO/Fe₃O₄ ternary nanocomposite, *Chem. Eng. J.*, 2021, **422**, 130159, DOI: **10.1016/j.cej.2021.130159**.